Journal of Molecular Structure 1108 (2016) 46–53

Contents lists available at ScienceDirect

Journal of Molecular Structure

journal homepage: http://www.elsevier.com/locate/molstruc

Computational and spectroscopic studies of the imidazole-fused phenanthroline derivatives containing phenyl, naphthyl, and anthryl groups

Jinglan Wang [a], Shengxian Xu [a], Feng Zhao [a, *], Hongying Xia [a, **], Yibo Wang [b]

[a] School of Chemistry and Chemical Engineering, Jiangxi Science and Technology Normal University, Fenglin Street, Nanchang, Jiangxi 330013, PR China
[b] Key Laboratory of Guizhou High Performance Computational Chemistry, Department of Chemistry, Guizhou University, Guiyang 550025, PR China

ARTICLE INFO

Article history:
Received 27 July 2015
Received in revised form
25 November 2015
Accepted 30 November 2015
Available online 10 December 2015

Keywords:
Ligand
Imidazo[4,5-f][1,10]phenanthroline
Density functional theory
Charge transfer
Photophysical property

ABSTRACT

Three N,N-bidentate ligands, 2-phenyl-1H-imidazo[4,5-f][1,10]phenanthroline (**1**), 2-(2-naphyl)-1H-imidazo[4,5-f]phenanthroline (**2**), and 2-(2-anthryl)-1H-imidazo[4,5-f]phenanthroline (**3**) have been synthesized and characterized. Effects of aryl subsistiuents (phenyl, naphthyl, and anthryl) on the photophysical properties of these ligands in solution have been studied. Ligand **1** exhibit the main absorption band at 283 nm with the shoulder bands at 300–350 nm and these bands are assigned as the typical $\pi\rightarrow\pi^*_{(imPhen)}$ state (imPhen = 1H-imidazo[4,5-f][1,10]phenanthroline). A similar absorption spectrum was also observed in the case of **2,** in which the charge transfer (CT) state should be considered. **3** shows the slightly different absorption properties compared to that of **1** and **2**. The highest-lying absorption band at 257 nm is assigned as a mixed $\pi\rightarrow\pi^*_{(imPhen)}/\pi\rightarrow\pi^*_{(Anth)}$ (Anth = anthracene) state. Additionally, the characteristic absorption band of anthryl group with three vibronic bands at 352, 367, and 386 nm also observed in the visible region range from 340 to 400 nm. **1** shows the typical ligand-centered $^1\pi\rightarrow\pi^*$ emission, while **2** and **3** emit from the mixed $^1\pi\rightarrow\pi^*$/CT states. Density functional theory (DFT) and time-dependent density functional theory (TDDFT) were employed to rationalize the photophysical properties of these ligands studied. The theoretical data confirm the assignment of the experimental absorption spectra and the nature of the emitting states.

1. Introduction

The transition metal complexes have received much current interest owing to their unique photophysical properties such as the MLCT visible absorption, relatively long-lived excited lifetimes, and high luminescence efficiency, and so on [1–5]. Their photophysical properties are sensitive to the coordinated ligand system and can easily be modulated by an appropriate choice and combination of ligands and ligand substituents. Until now, the number of ligands with different structural and electronic properties have been designed and synthesized in order to tune the photophysical properties of these complexes [6–12]. Among them, the most commonly used ligands are based on 1,10-phenanthroline (Phen) due to their rigid planar, hydrophobic, electro-poor heteroaromatic system [13,14]. Additionally, the utilization of the functionalized Phen or its derivatives provides further options to tune the optical and electrical properties [15–20].

As a Phen derivative, 1H-imidazo[4,5-*f*][1,10]phenanthroline (imPhen) is an appealing ligand [21,22]. The fused imidazole ring provides a more π-delocalized molecular skeleton, and consequently has a positive impact on the photophysical proprieties of the corresponding complexes. Meanwhile, imPhen ligands can be easily substituted with electron-withdrawing or –donating groups, and these substitutions have an important effect on their HOMO and LUMO energies and consequently on the corroding metal complex emission. A large number of metal complexes of imPhen such as those of Ru(II), Ir(III), Pt(I), Re(I), and Cu(I), have been reported and shown interesting photophysical properties [23–30]. However, the electrical structures and the photophysical properties of these ligands seem deficient compared to that of Phen [31,32] and the origin of these spectroscopic properties remains unexplored. Therefore, a deep understanding of fundamental

* Corresponding author.
** Corresponding author.
E-mail addresses: zhf19752003@163.com (F. Zhao), xiahongying85@sohu.com (H. Xia).

http://dx.doi.org/10.1016/j.molstruc.2015.11.082
0022-2860/

photophysical properties of imPhen ligand with new molecular structures is desired to furthermore guide the future molecular design of new complexes.

Herein, the photophysical properties of three imPhen derivatives with phenyl, naphthyl, and anthryl groups (Chart 1) were studied by exploiting their optical absorption and photoluminescent spectra. The emphasis is being given a detailed analysis of the structural and spectral properties of those ligands. Meanwhile, the assignment of the electronic absorption and emission spectra were also investigated using density functional theory (DFT) and time-dependent density functional theory (TDDFT), and the results are compared with the corresponding experimental data.

2. Experimental

2.1. Materials and methods

1,10-phenanthroline (Phen), 2,9-dimethyl-1,10-phenanthroline, Ethylenediamine, Potassium bromide were purchased from Aladdin-reagent Co. and used without further purification. Concentrated sulfuric and nitric acids were purchased from Sinopharm Chemical Reagent Co. The solvent dichloromethane used for UV–vis absorption and emission spectroscopy was obtained from Shanghai Vita Chemical Reagent Co., Ltd (99.9%. HPLC grade). ^{1}H NMR spectra were performed in a Bruker AV400 MHz spectrometer, using tetramethylsilane (TMS) as internal reference. DMSO-d_6 was used as the solvents. UV–vis absorption spectra were measured using a Perkin Elmer Lambda-900 spectrophotometer. Fluorescence spectra were determined with a Hitachi F-4500 fluorescence spectrophotometer. Photoluminescence (PL) quantum yields were determined using a Hamamatsu system for absolute PL quantum yield measurements (type C11347). Fluorescent lifetimes were measured with a compact fluorescent lifetime spectrometer (Hamamatsu, C11367, Japan).

2.2. Synthetic procedure

2.2.1. 2,9-Dimethyl-1,10-Phenanthroline-5,6-dione

A round-bottom flask containing 2,9-dimethyl-1,10-phenanthroline (3.35 g, 16 mmol) and potassium bromide (19.0 g, 160 mmol) was cooled in an ice bath. Concentrated sulfuric acid (60 mL) and concentrated nitric acid (30 mL) were added dropwise. The reaction mixture was heated under reflux for 3 h, then cooled to room temperature and the solution poured slowly into deionized water (800 mL), neutralized with sodium bicarbonate and extracted with CH_2Cl_2. After washed with water and dried, the chloroform was removed under reduced pressure to leave a yellow residue which was recrystallized from dioxane. Yield: 78% (3.5 g). ^{1}H NMR (400 MHz, DMSO-d_6): 8.20–8.22 (dd, 2H), 8.59–8.61 (dd, 2H), 2.82 (s,6H).

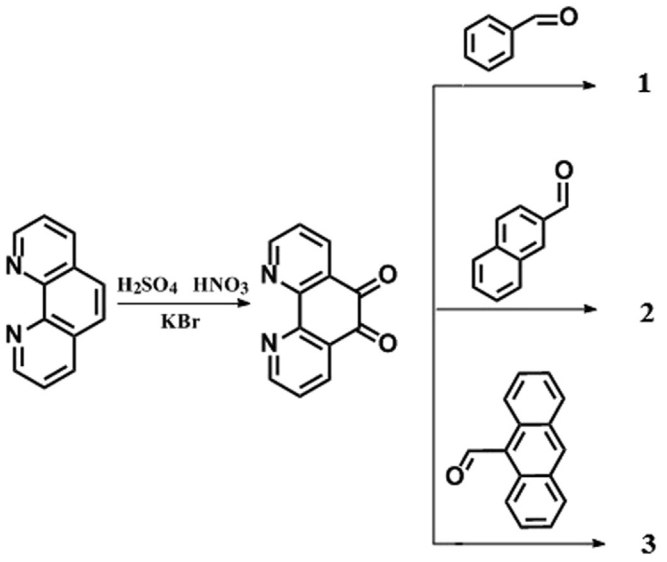

Scheme 1. The synthetic pathways of ligands.

2.2.2. 2-phenyl-1H-imidazo[4,5-f][1,10]phenanthroline (*1*)

A mixture of 1,10-Phenanthroline-5,6-dione (104 mg, 0.50 mmol), benzaldehyde (72 mg, 0.68 mmol), ammonium acetate (805 mg, 11.3 mmol), and glacial acetic acid (13 mL) was refluxed for 4 h and then cooled to room temperature. It was diluted with water and dropwise addition of concentrated aqueous ammonia gave a yellow precipitate, which was collected, washed with water, and dried. The crude product obtained was purified by chromatography on silica gel, prepared in a 8:1 mixture of CH_2Cl_2 and methanol. Yield: 96 mg (65%). ^{1}H NMR (400 MHz, DMSO): 13.76 (s, 1H)9.02 (d, J = 8.0 Hz, 2H), 8.93 (d, J = 8.0 Hz, 2H), 8.29 (d, J = 7.9 Hz, 2H), 7.82 (dd, J = 7.9, 4.4 Hz, 2H), 7.61 (t, J = 7.5 Hz, 2H), 7.51 (t, J = 7.2 Hz, 1H).

2.2.3. 2-(2-naphyl)-1H-imidazo[4,5-f]phenanthroline (*2*)

The synthetic procedure was the same as that for compound **1** except for that 106 mg (0.68 mmol) 2-naphthaldehyde was used for the reaction. Yiedl: 95 mg (55%). ^{1}H NMR (400 MHz, DMSO-d_6): 13.76 (s, 1H) 9.10–9.02 (m, 2H), 8.98 (d, *J* = 7.2 Hz, 2H), 8.83 (s, 1H), 8.45 (d, *J* = 8.5 Hz, 1H), 8.14 (dd, *J* = 16.6, 8.0 Hz, 2H), 8.03 (d, *J* = 8.4 Hz, 1H), 7.86 (dd, *J* = 7.9, 4.2 Hz, 2H), 7.63 (p, *J* = 8.4 Hz, 2H).

2.2.4. 2-(9-anthryl)-1H-imidazo[4,5-f]phenanthroline (*3*)

The synthetic procedure was the same as that for **1** except for that 140.2 mg (0.68 mmol) 9-anthrylaldehyde was used for the reaction and the reaction mixture was refluxed for 6 h. Yiedl: 89 mg (45%). ^{1}H NMR (400 MHz, DMSO-d_6): 14.16 (s, 1H), 9.02 (d, J = 4.1 Hz, 2H), 8.90 (d, J = 8.1 Hz, 1H), 8.85 (s, 1H), 8.72 (d, J = 7.3 Hz, 1H), 8.20 (d, J = 8.4 Hz, 2H), 7.79 (dd, J = 8.0, 4.4 Hz, 2H), 7.74 (d, J = 8.7 Hz, 2H), 7.60–7.52 (m, 2H), 7.52–7.44 (m, 2H).

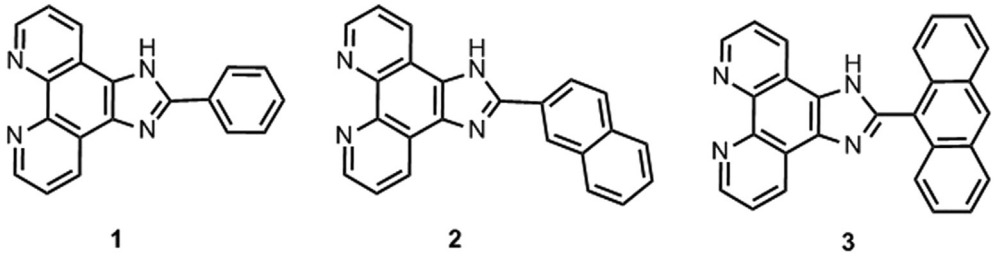

Chart 1. Molecular structures of the phenanthroline derivates studied in this study.

2.3. DFT calculations

All calculations were performed using the Gaussian 09 [33] program package. The B3LYP exchange-correlation function [34,35] with 6-31G* basis set [36,37] was used to optimize the ground state (S_0 state) geometries and the excited state geometries (S_1 state) of ligands **1**–**3** using the polarized continuum model (PCM) [38] in CH_2Cl_2 media. On the basis of the optimized ground geometries, TDDFT method [39,40] associated with PCM in CH_2Cl_2 media were used to simulate the absorption spectra of compounds **1**–**3**. The first 100 singlet vertical excitations were obtained form the TDDFT output file to construct the calculated absorption spectra. The calculated fluorescence emission energies of compounds **1**–**3** were obtained by TDDFT calculations based on the optimized singlet excited state geometries at the same level of theory used for geometrical optimization. Calculated electronic density plots for the frontier molecular orbitals were prepared using Gauss View 4.1.2 software and the molecular orbital compositions are calculated using Multiwfn analyzer soft [41].

3. Results and discussion

3.1. Synthesis

The synthetic pathways of the ligands **1**–**3** are shown in Scheme 1. 1,10-Phenanthroline-5,6-dione was synthesized according to a modified literature procedure [42]. These ligands were prepared by a condensation reaction according to the literature procedure [43].

Fig. 1 shows the UV–Vis spectra of **1**–**3** in CH_2Cl_2 solution at room temperature and the corresponding absorbance values of the relevant bands are shown in Table 1. In both **1** and **2**, the main absorption bands between 250 and 300 nm are assigned to the $\pi\rightarrow\pi^*$ transitions involving in imPhen moiety. In addition, both ligands also have low-energy bands (shoulder around 300–400 nm) that can be ascribed to the $\pi\rightarrow\pi^*$ states of imPhen moiety. However, the low-energy bands of **2** is red-shifted compared to **1**, attributing to the extended π-conjugation in **2** due to the introduction of the naphthyl moiety. Ligand **3** displays different absorption properties: a high-energy band localized at 257 nm is much narrower than that of ligands **1** and **2**. This indicates that the contribution of the anthryl-centered $\pi\rightarrow\pi^*$ transition is also present for this bands besides that of the imPhen-based $\pi\rightarrow\pi^*$ transition. The shoulder at 284 nm is assigned to the anthryl-centered $\pi\rightarrow\pi^*$ state with partial charge-transfer character (CT) from the anthryl group to imPhen moiety. The assignments of these bands are supported by TDDFT calculations (see below). The characteristic absorption band of anthryl group with three vibronic bands at 352, 367, and 386 nm also observed in the visible region range from 340 to 400 nm in the spectrum of **3** (see inset in Fig. 1), which is consistent with that reported in literature [44,45].

Table 1
Photophysical properties of **1, 2,** and **3**.

	Absorption	Emission				
	λ_{abs}/nm	λ_{em}/nm	τ/ns	Φ/%	$k_r/10^7 s^{-1}$	$k_{nr}/10^8 s^{-1}$
1	282, 306, 322 (sh)	423	5.7	2.9	0.51	1.7
2	273, 332, 348 (sh)	430	6.1	5.5	0.90	1.5
3	257, 284 (sh), 352, 367, 386	510	11.1	7.0	0.63	0.8

The normalized fluorescence emission spectra of **1**–**3** in CH_2Cl_2 solution are shown in Fig. 2. **1** displays the fluorescence emission at 423 nm with slightly vibrational structure at around 525 nm, clearly indicating an emitting state of the imPhen-centered $\pi\rightarrow\pi^*$ character. For **2**, the main change on the shape of the emission spectrum is that the vibrational structure vanishes and the reasons for this behavior would be consistent with a somewhat greater contribution of CT character into the $\pi\rightarrow\pi^*$ emissive state. Further confirmation of the emissive state is provide in the theoretical description of **2** (see 3.5 section). For **3**, the shape of the emission spectrum resembles that of **2**, but, the emission band maximum is significantly red-shifted to 510 nm, meaning that **3** also have a mixed $\pi\rightarrow\pi^*$/CT character but with the different contribution proportion of $\pi\rightarrow\pi^*$ and CT states. The different nature of the emitting states is also reflected in the photoluminescence quantum yields (PLQY) and excited-state lifetimes. **1**, **2**, and **3** show quantum yields of 2.9, 5.5, and 7.0%, respectively, together with excited state lifetimes of 5.7, 6.1, and 11.1 ns (see Table 1). The radiative rate constant, k_r, of **1** ($0.51 \times 10^7\ s^{-1}$) is smaller than that of 2 and 3 ($0.90 \times 10^7\ s^{-1}$ and $0.63 \times 10^7\ s^{-1}$, respectively), which is due to the change of the nature of the emissive state from a $\pi\rightarrow\pi^*$ transition for **1** to a mixed $\pi\rightarrow\pi^*$/CT transition for **2** and **3**.

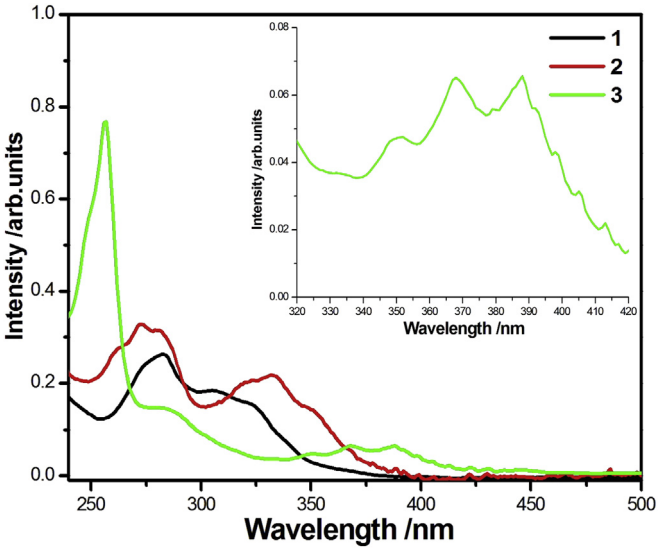

Fig. 1. Absorption spectra in dichloromethane at 298 K of ligands **1**–**3**. (inset) the region of 320–420 nm is magnified to allow easy comparison.

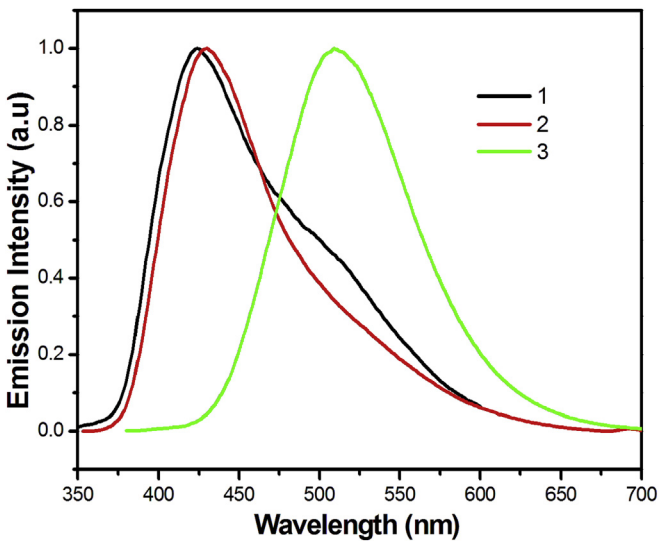

Fig. 2. Normalized emission spectra of **1**–**2** in dichloromethane solution.

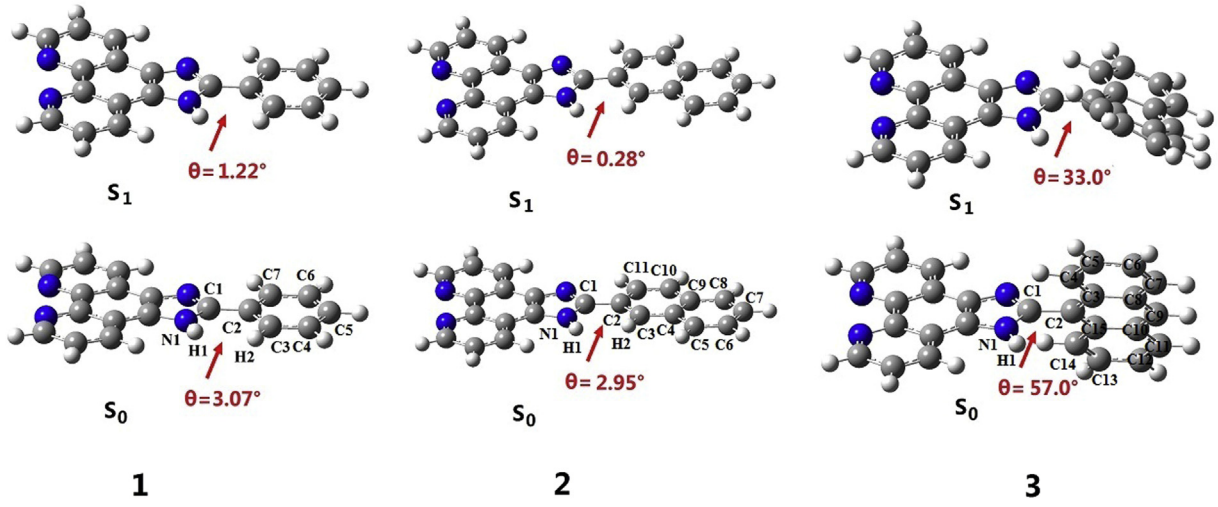

Fig. 3. Optimized ground state and the singlet excited state geometric structures of **1**–**3**.

Table 2
Frontier molecular orbital compositions (%) for **1** the ground state in CH_2Cl_2 solution at the B3LYP/6-31G* level.

Orbital	Energy(ev)	Main bond type	Contribution (%)	
			imPhen	Ph
L+3	−0.23	π*(Ph)	1.50	98.5
L+2	−1.06	π*(imPhen)	77.2	22.8
L+1	−1.41	π*(imPhen)	83.4	16.6
L	−1.53	π*(imPhen)	89.2	10.8
HOMO-LUMO gap (4.14 ev)				
H	−5.67	π(imPhen)	81.9	19.1
H-1	−6.52	π(imPhen)	98.7	1.33
H-2	−6.80	π(imPhen)	99.9	0.04
H-3	−7.07	π(Ph)	4.7	95.3

Table 3
Frontier molecular orbital compositions (%) for **2** the ground state in CH_2Cl_2 solution at the B3LYP/6-31G* level.

Orbital	Energy(ev)	Main bond type	Contribution (%)	
			imPhen	Naph
L+3	−0.84	π*(Naph)+ π*(imPhen)	22.4	78.6
L+2	−1.16	π*(imPhen)	84.0	16.0
L+1	−1.48	π*(imPhen)	95.6	4.44
L	−1.68	π*(Naph) + π*(imPhen)	48.2	51.8
HOMO-LUMO gap (3.92ev)				
H	−5.60	π(imPhen)+π (Naph)	67.1	32.9
H-1	−6.23	π(Naph)	15.8	84.2
H-2	−6.53	π(imPhen)	98.3	1.72
H-3	−6.80	π(imPhen)	99.1	0.04

3.2. Ground state geometries and molecular orbital properties

The optimized ground state geometric structures (S_0 state) of the all ligands are shown in Fig. 3. Vibrational frequencies were calculated based on these optimized geometries to verify that the geometries represented a minimum on the potential energy surface. The N1−C1−C2−C3 dihedral angles of **1** and **2** display small variability ($\theta = 3.07^\circ$ for **1**, $\theta = 2.95^\circ$ for **2**, see Fig. 3 for the atom numbering). However, the torsion angle between anthryl group and imidazole ring is larger for **3** than for **1** and **2** ($\theta = 57.0^\circ$ for **3**), indicating the present of the steric repulsion between the H1 imidazole ring and H2 atom of the anthryl group.

The frontier molecular orbital compositions for the all ligands have been analyzed using Multiwfn analyzer soft [39] and are listed in Tables 2–4. Fig. 4 shows the energy levels and plots of the main molecular orbitals of interest in **1**–**3**. For **1**, the highest occupied molecular orbitals (HOMO) largely resides on the imPhen moiety, and the composition extends to the phenyl group with the proportion of 19.1%. The HOMO of **2** has the similar distribution to **1** only with different orbital compositions. The extended π-conjugation across the imPhen moiety and the naphthyl ring pulls the electron density moving toward the naphthyl ring with the increasing proportion of up to 32.9%. For **3**, the orbital compositions of the HOMO change significantly compared with that in **1** and **2**. The electron densities are mainly localized in the anthryl group (78.1%), rather than the imPhen moiety (22.9%). The main reason is due to the torsion angle of 57.0° between the imPhen moiety and the anthryl ring, which breaks the π-conjugation across the imPhen moiety and the anthryl ring to a large extent and results in the shift of the electron density from the imPhen moiety to the anthryl group. The electron densities of the lowest unoccupied molecular orbitals (LUMO) of **1**–**3** are greatly influenced by different aryl groups. The contribution of aryl groups gradually increased from the phenyl to anthryl group. The LUMO of **1** is composed of 89.2% π*(imPhen) and 10.8% π*(Ph), while that of **2** is localized on 48.2% π*(imPhen) and 51.8% π*(Naph). But with respect to the LUMO of **3**, the contribution from the anthryl group is increased to 91.8%. These results explain why the various aryl groups have effect on the

Table 4
Frontier molecular orbital compositions (%) for **3** the ground state in CH_2Cl_2 solution at the B3LYP/6-31G* level.

Orbital	Energy(ev)	Main bond type	Contribution (%)	
			imPhen	Anth
L+4	−0.54	π*(Anth)+ π*(imPhen)	51.9	48.1
L+3	−0.58	π*(Anth)+ π*(imPhen)	34.7	65.3
L+2	−1.27	π*(imPhen)	96.4	3.57
L+1	−1.50	π*(imPhen)	98.0	2.02
L	−2.02	π*(Anth)	8.20	91.8
HOMO-LUMO gap (3.37ev)				
H	−5.39	π(Anth)	22.9	78.1
H-1	−6.06	π(imPhen)	75.2	24.8
H-2	−6.54	π(imPhen)	98.1	1.93
H-3	−6.74	π(Anth)	0.8	99.2
H-6	−7.25	π(imPhen)	98.6	1.37
H-7	−7.59	π(imPhen)	95.5	4.53

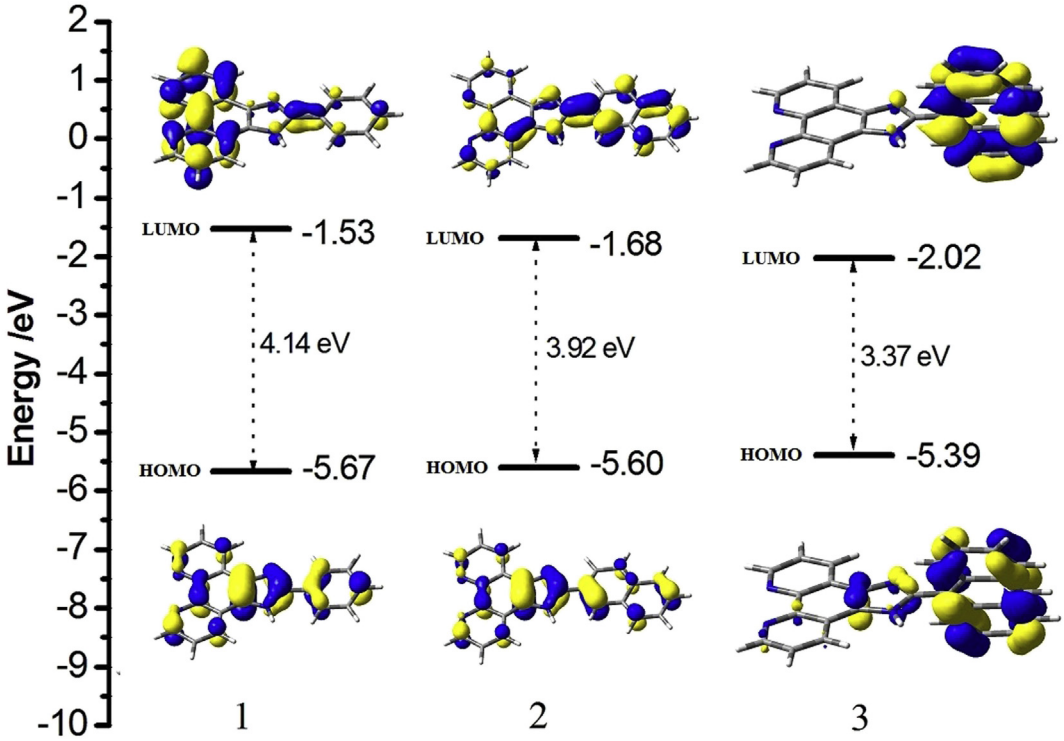

Fig. 4. Energy levels and the energy values calculated for the molecular orbitals of **1**–**3** with representative contour plots of the molecular orbitals.

energy levels of the HOMO and LUMO. Upon replacing the phenyl group by the naphthyl group the HOMO energy of **2** is slightly destabilized by 0.07 eV compared to that of **1**, whereas the LUMO energy is strongly stabilized by 0.15 eV since the LUMO of **2** has a much larger amount of electron density on the naphthyl ring than that of **1**. With respect to **3**, both the HOMO and LUMO have substantial electron density on the anthryl group and hence the attachment of the anthryl groups to imPhen moiety has strong influence on both the HOMO and LUMO. The HOMO energy of **3** is destabilized by 0.28 eV, while the LUMO is stabilized by 0.49 eV

Table 5
Electronic absorptions of complexes **1**–**3** in CH_2Cl_2 based on TDDFT calculations at the (B3LYP)/6-31g* level, together with the experimental values.

	Excited state	Transition	Coeff	E(eV)/(nm)	*f*	Assign[a]	Exptl/nm
1	2	H→L+1	0.63725(81.2%)	3.79/327	0.4934	$\pi\rightarrow\pi^*_{(imPhen)}$	322
	3	H→L+2	0.65698(86.3%)	4.04/307	0.3254	$\pi\rightarrow\pi^*_{(imPhen)}$	306
	7	H-1→L	0.58274(67.9%)	4.61/269	0.5322	$\pi\rightarrow\pi^*_{(imPhen)}$	282
2	1	H→L	0.59761(71.4%)	3.48/357	0.5404	$\pi\rightarrow\pi^*_{(imPhen)}/LLCT_{(imPhen\ \rightarrow\ Naph)}$	348
		H→L+1	−0.35113(24.7%)			$\pi\rightarrow\pi^*_{(imPhen)}/LLCT_{(Naph\ \rightarrow\ imPhen)}$	
	2	H→L+1	0.59142(70.0%)	3.58/346	0.3222	$\pi\rightarrow\pi^*_{(imPhen)}/LLCT_{(Naph\ \rightarrow\ imPhen)}$	332
		H→L	0.35822(25.7%)			$\pi\rightarrow\pi^*_{(imPhen)}/LLCT_{(imPhen\ \rightarrow\ Naph)}$	
	10	H-2→L+1	0.50452(50.9%)	4.55/273	0.3631	$\pi\rightarrow\pi^*_{(imPhen)}$	273
		H-1→L+2	0.33708(22.7%)			$LLCT_{(Naph\ \rightarrow imPhen)}$	
		H→L+2	−0.22073(9.74%)			$\pi\rightarrow\pi^*_{(imPhen)}/LLCT_{(Naph\ \rightarrow\ imPhen)}$	
3	1	H→L	0.70025(98.1%)	2.99/415	0.3067	$\pi\rightarrow\pi^*_{(Anth)}$	352,367,386
	10	H→L+4	0.51668(53.4%)	4.28/290	0.0983	$\pi\rightarrow\pi^*_{(Anth)}/LLCT_{(Anth\ \rightarrow\ imPhen)}$	284
		H→L+3	−0.40634(33.0%)			$\pi\rightarrow\pi^*_{(Anth)}/LLCT_{(Anth\ \rightarrow\ imPhen)}$	
	16	H-2→L+1	0.48177(46.4%)	4.67/266	0.4240	$\pi\rightarrow\pi^*_{(imPhen)}$	257
		H-1→L+2	0.29305(17.2%)			$\pi\rightarrow\pi^*_{(imPhen)}$	
		H-6→L+1	−0.27480(15.1%)			$\pi\rightarrow\pi^*_{(imPhen)}$	
	17	H-3→L	0.36344(26.4%)	4.76/260	0.7221	$\pi\rightarrow\pi^*_{(Anth)}$	
		H→L+3	0.34747(24.1%)			$\pi\rightarrow\pi^*_{(Anth)}/LLCT_{(Anth\ \rightarrow\ imPhen)}$	
		H→L+4	0.28819(16.6%)			$\pi\rightarrow\pi^*_{(Anth)}/LLCT_{(Anth\ \rightarrow\ imPhen)}$	
		H-1→L+3	0.28100(15.8%)			$\pi\rightarrow\pi^*_{(imPhen)}/LLCT_{(imPhen\ \rightarrow\ Anth)}$	
	23	H-1→L+4	0.36540(26.7%)	5.07/245	0.6053	$\pi\rightarrow\pi^*_{(imPhen)}/LLCT_{(imPhen\ \rightarrow\ Anth)}$	
		H-1→L+3	−0.35493(25.2%)			$\pi\rightarrow\pi^*_{(imPhen)}/LLCT_{(imPhen\ \rightarrow\ Anth)}$	
		H-7→L	−0.28847(16.6%)			$LLCT_{(imPhen\ \rightarrow\ Anth)}$	
		H-2→L+2	0.27118(14.7%)			$\pi\rightarrow\pi^*_{(imPhen)}$	
	26	H-1→L+4	0.40989(33.6%)	5.13/242	0.9814	$\pi\rightarrow\pi^*_{(imPhen)}/LLCT_{(imPhen\ \rightarrow\ Anth)}$	
		H-3→L+2	0.31838(20.3%)			$LLCT_{(Anth\ \rightarrow\ imPhen)}$	
		H-3→L	−0.24952(12.5%)			$\pi\rightarrow\pi^*_{(Anth)}$	
		H-1→L+3	0.24396(11.9%)			$\pi\rightarrow\pi^*_{(imPhen)}/LLCT_{(imPhen\ \rightarrow\ Anth)}$	

[a] The actual percent contribution=(configuration coefficient)^2 × 2 × 100%.

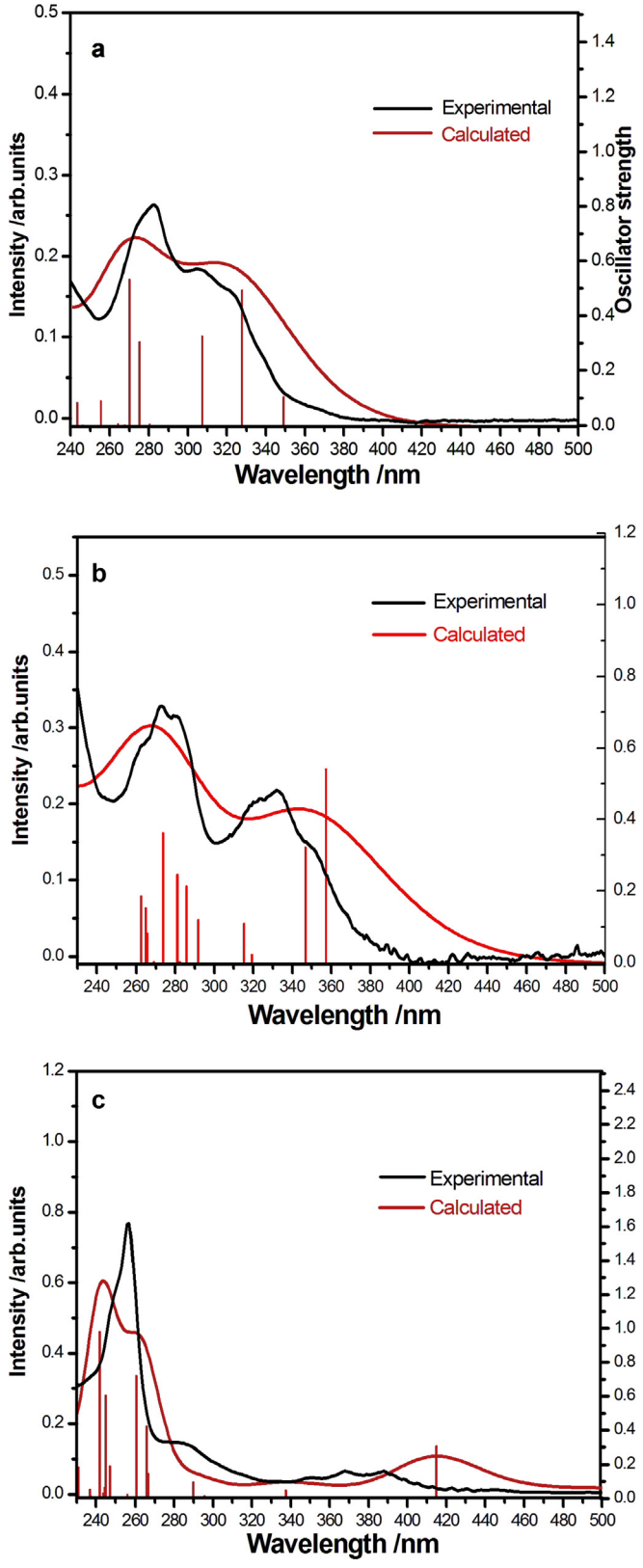

Fig. 5. Comparison of the calculated (red line) and experimental (black line) absorption spectra in CH_2Cl_2 solution for **1** (a), **2** (b), and **3**(c). Red vertical lines correspond to oscillator strength of calculated singlet–singlet transitions. (For interpretation of the references to colour in this figure legend, the reader is referred to the web version of this article.)

compared to that of **1**. The calculated HOMO-LUMO energy gap decreases in the order: **1**(4.14 eV) > **2**(3.92 eV) > **3**(3.37 eV), in reasonably good agreement with the red shift of the lowest energy absorption maxima observed in the experiments.

3.3. Theoretical absorption spectra

To gain insight into the transition character of absorption spectra of the all ligands, TDDFT calculations were undertaken to simulate the absorption spectra. Table 5 lists the dominant energy singlet–singlet vertical excitations, their oscillator strengths (*f*), assignment configurations, and excitations with maximum coefficients. A comparison of calculated and experimental absorption spectra for **1**–**3** is presented in Fig. 5.

For **1**, we calculate three intense excitation transitions at 269, 307, and 327 nm (f = 0.5322, 0.3254, and 0.4934), in good agreement with the experimental values at 283, 306, and 322 nm, respectively. The 269 nm absorption band mainly originates form the transition of HOMO-1→LUMO (67.9%). The HOMO-1 mainly consists of π(imPhen) (98.7%), whereas the LUMO are predominantly composed of π^*(imPhen) (89.2%) (see Table 1). Thus, this band can be assigned to $\pi \rightarrow \pi^*_{(imPhen)}$ transition in character. The 307 nm band should be assigned to HOMO [π(imPhen)]→LUMO+2 [π^*(imPhen)] transition with $\pi \rightarrow \pi^*_{(imPhen)}$ character. In addition, the 327 nm band has the similar $\pi \rightarrow \pi^*_{(imPhen)}$ character, originating from the HOMO-→LUMO+1 transition. The main spectral features in experiments are well reproduced by our TDDFT calculation.

With respect to **2**, the highest-lying absorption band calculated at 273 nm, which corresponds well to the experimental value of 272 nm, appears to mainly originate from the transition of HOMO-2 [π(imPhen)]→LUMO+1 [π^*(imPhen)] (50.9%) with $\pi \rightarrow \pi^*_{(imPhen)}$ character, along with some contribution from the HOMO-1 [π(Naph)] →LUMO+2 [π^*(imPhen)] (22.7%) with ligand-to ligand charge transfer (LLCT) character. The calculated excitation transitions at 346 nm originated from the HOMO→LUMO+1 (70.0%)/LUMO (25.7%) transition with the oscillator strength of $f = 0.3222$ and 357 nm originated from the HOMO→LUMO (71.4%)/LUMO+1 (24.7%) transition with the oscillator strength of $f = 0.5404$ can be related to the 332 and 351 nm features of the experimental spectrum (Fig. 5b). These bands have mixed $\pi \rightarrow \pi^*_{(imPhen)}$ and LLCT characters.

For **3**, the high-energy region is dominated by four primary excitation transitions at 242, 245, 260, and 266 nm ($f = 0.9814$, 0.6053, 0.7221, and 0.4240), to be correlated with the experimental peak at 257 nm. These transitions can be described as mixed $\pi \rightarrow \pi^*_{(imPhen)}/\pi \rightarrow \pi^*_{(Anth)}$ characters. The results support clearly our assignment of the high-energy absorption band of **3** made above. It should be stressed that the some CT contribution between imPhen moiety and anthryl group is also responsible for the high-energy absorption bands as shown in Table 3. A lower intense transition calculated at 290 nm originating from the HOMO-→LUMO+4 (53.4%)/LUMO+3 (33.0%) with the oscillator strength of $f = 0.0983$ is the closest in energy to the experimental shoulder at 284 nm and is assigned as $\pi \rightarrow \pi^*_{(Anth)}$ state with LLCT character from anthryl group to imPhen moiety. The calculated absorption band at 415 nm with the larger oscillator strength of $f = 0.3067$ is dominantly originated from the H [π(Anth)] → L [π^*(Anth)] transition with $\pi \rightarrow \pi^*_{(Anth)}$ character, corresponding well to the experimental absorption bands in the range of 350–400 nm considering the rather limited dimensions of the basis set and the approximate nature of solvent model, even though the calculated spectra do not display vibronic fine structure of anthryl group.

3.4. Singlet excited state geometries and emission properties

According to Kasha's rule, the fluorescence of the molecules only

Table 6
Plots of fluorescence emission transitions calculated for **1**–**3** at CH_2Cl_2 solution.

	λ_{em} (eV)/(nm)	Transition(percent contribution[a])	Assignment	Exptl (eV)/(nm)
1	3.16/392	LUMO→HOMO(94.4%)	$\pi\rightarrow\pi^*_{(imPhen)}$	2.93/423
2	3.08/402	LUMO→HOMO(97.2%)	$\pi\rightarrow\pi^*_{(imPhen)}$/CT	2.89/430
3	2.20/562	LUMO→HOMO(100%)	$\pi\rightarrow\pi^*_{(imPhen)}$/CT	2.43/510

[a] The actual percent contribution=(configuration coefficient)^2 × 2 × 100%.

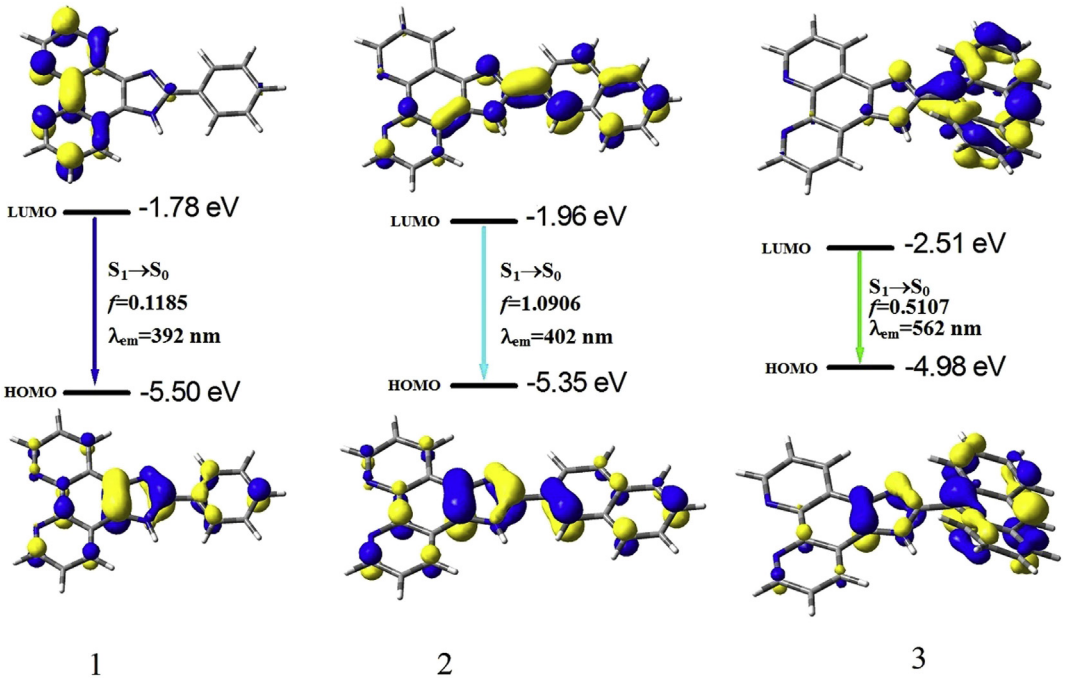

Fig. 6. Plots of emission transitions calculated in TDDFT level of **1**–**3**.

emit from the lowest singlet excited states instead of the high-lying S_n excited states. Thus, the singlet excited state geometries of **1**–**3** were optimized and the corresponding structures are also shown in Fig. 3. For **1** and **2**, the slight difference of the S_1 structures compared to S_0 is the change of the dihedral angle between aryl group and imPhen ring. That is, phenyl and naphthyl rings are more planar with imPhen ring in the S_1 state. However, the co-planarity within the anthryl and imPhen rings is substantially distorted because of the steric repulsions between the atom H1of the imPhen ring and the atom H2 of anthryl groups. The remarkable geometry difference between S_0 and S_1 states for **3** may be responsible for the large red-shift of emission wavelength compared with that of **1** and **2** in the experiments. In order to gain insight into the nature of the emissive excited states, the fluorescence emission energies of **1**–**3** were calculated using TDDFT method at their respective S_1 geometry. The results of the TDDFT calculations are listed in Table 6 and the plots of frontier molecular orbitals related to emission of **1**–**3** are presented in Fig. 6. The fluorescence emission wavelengths calculated at 392, 402, and 562 nm for **1**–**3** reasonably agree with the experimental values of 423, 430, and 510 nm, respectively. For **1**, the emission at 392 nm ($S_1\rightarrow S_0$) is contributed by the excitation transition of LUMO→HOMO. The HOMO is largerly distributed on the imPhen ligand (78.2%) with little contribution from phenyl group (21.1%) in the S_1 state (the distributions of the orbital compositions in the singlet excited state are provided in Table 1S, Supporting Information), while the LUMO is a π^* orbital on the imPhen ligand (94.2%), thus the emission at 392 nm is mainly ascribed as $\pi\rightarrow\pi^*_{(imPhen)}$ state. The fluorescence emission at 402 nm of **2** is originated from the LUMO[π^*(Naph) (53.2%)+π^*(imPhen) (46.8%)] →HOMO[π(imPhen) (65.1%)] with $\pi\rightarrow\pi^*_{(imPhen)}$/CT character. The theoretical results support clearly our assignment of the nature of the emitting state of **2** discussed above. With respect to **3**, the LUMO[π^*(Anth) (78.8%)]→HOMO [π(Anth) (63.4%)+π^*(imPhen) (36.6%)] transition with $\pi\rightarrow\pi^*_{(Anth)}$/CT character, in which the $\pi\rightarrow\pi^*_{(Anth)}$ state seem to predominate, is responsible for the emission calculated at 562 nm.

4. Conclusion

In this paper, three imidazole-fused phenanthroline derivatives, 2-phenyl-1H-imidazo[4,5-f][1,10]phenanthroline (**1**), 2-(2-naphyl)-1H-imidazo[4,5-f]phenanthroline (**2**), and 2-(2-anthryl)-1H-imidazo[4,5-f]phenanthroline (**3**), were synthesized and characterized. The absorption and luminescence properties of these ligands are investigated in the experiments and the assignments of the absorption bands and the emitting states are interpreted in detail with the aid of DFT and TDDFT calculations. The results show that the main absorption bands in the UV for **1** are assigned as $\pi\rightarrow\pi^*$ transitions, while **2** and **3** exhibit the similar transition character but with partial CT character. In addition, **1** shows $^1\pi\rightarrow\pi^*$ emission, whereas 2 and 3 emit from the mixed $^1\pi\rightarrow\pi^*$/CT state. These experimental and theoretical insights should be expected to provide some guides for the design and synthesis of new ligands and the corresponding complexes.

Acknowledgments

The work was supported by the National Natural Science

Foundation of China (Nos.21462020, 21443010, and 21563013), Jiangxi Science and Technology Normal University Key Laboratory of Organic-inorganic Composite Materials (Key training base) (No.300098010303), and the Natural Science Foundation of Jiangxi Province (No. 20151BAB203006). The authors thank the Guizhou University High Performance Computation Chemistry Laboratory (GHPCC) for help with computational studies.

Appendix A. Supplementary data

Supplementary data related to this article can be found at http://dx.doi.org/10.1016/j.molstruc.2015.11.082.

References

[1] H. Yersin, Top. Curr. Chem. 241 (2004) 1.
[2] M. Mazzeo, V. Vitale, F. Della Sala, M. Anni, G. Barbarella, L. Favaretto, G. Sotgiu, R. Cingolani, G. Gigli, Adv. Mater. 17 (2005) 34.
[3] Y. Chi, P.T. Chou, Chem. Soc. Rev. 39 (2010) 638.
[4] B. Happ, A. Winter, M.D. Hager, U.S. Schubert, Chem. Soc. Rev. 41 (2012) 2222.
[5] V.W.W. Yam, K.M.C. Wong, Chem. Comm. 47 (2011) 11579.
[6] B. Ma, P.I. Djurovich, M.E. Thompson, Coord. Chem. Rev. 249 (2005) 1501.
[7] R. Visbal, M.C. Gimeno, Chem. Soc. Rev. 43 (2014) 3551.
[8] R.D. Costa, E. Orti, H.J. Bolink, F. Monti, G. Accorsi, N. Armaroli, Angew. Chem. Int. 51 (2012) 8178.
[9] Y. Chi, B.H. Tong, P.T. Chou, Coord. Chem. Rev. 281 (2014) 1.
[10] S. Serroni, S. Campagna, F. Puntoriro, C. Di Pietro, N.D. McClenaghan, F. Loiseau, Chem. Soc. Rev. 30 (2001) 367.
[11] L.A. Sacksteder, A.P. Zipp, E.A. Brown, J. Streich, J.N. Demas, B.A. DeGraff, Inorg. Chem. 29 (1990) 4335.
[12] C. Bizzarri, C. Strabler, J. Prock, B. Trettenbrein, M. Ruggenthaler, C.H. Yang, F. Polo, A. Iordache, P. Bruggeller, L.D. Cola, Inorg. Chem. 53 (2014) 10944.
[13] G. Accorsi, A. Listorti, K. Yoosaf, N. Armaroli, Chem. Soc. Rev. 38 (2009) 1690.
[14] A. Bencini, V. Lippolis, Coord. Chem. Rev. 254 (2010) 2096.
[15] H.S. Joshi, R. Jamshidi, Y. Tor, Angew. Chem. Int. 38 (1999) 2721.
[16] N. Armaroli, Chem. Soc. Rev. 30 (2001) 113.
[17] Z.A. Siddique, Y. Yamamoto, T. Ohno, K. Nozaki, Inorg. Chem. 42 (2003) 6366.
[18] M.T. Miller, P.K. Gantzel, T.B. Karpishin, Inorg. Chem. 38 (1999) 3414.
[19] C.E. McCusker, F.N. Castellano, Inorg. Chem. 52 (2013) 8114.
[20] E.C. Riesgo, X.Q. Jin, R.P. Thummel, J. Org. Chem. 61 (1996) 3017.
[21] H. Chao, R.H. Li, B.H. Ye, H. Li, X.L. Feng, J.W. Cai, J.Y. Zhou, L.N. Ji, J. Chem. Soc. Dalton Trans. (1999) 3711.
[22] T. Cardinaels, J. Ramaekers, P. Nochemann, K. Driesen, K.V. Hecker, L.V. Meervelt, S.B. Lei, S.D. Feyter, D. Guillon, B. Donnio, K. Binnemans, Chem. Mater. 20 (2008) 1278.
[23] M.J. Han, L.H. Gao, K.Z. Wang, New. J. Chem. 30 (2006) 208.
[24] X.Y. Yi, P. Yang, D.D. Huang, J.Z. Zhao, Dyes Pigm. 96 (2013) 104.
[25] Q. Zhao, S.J. Liu, M. Shi, F.Y. Li, H. Jing, T. Yi, C.H. Huang, Organometallics 26 (2007) 5922.
[26] K.J. Castor, J. Mancini, J. Fakhoury, N. Weill, R. Kieltyka, P. Englebienne, N. Avakyan, A. Mittermaier, C. Autexier, N. Moitessier, H.F. Sleiman, Chem. Med. Chem. 7 (2012) 75.
[27] R.O. Bonello, I.R. Morgan, B.R. Yeo, L.E.J. Jones, B.M. Kariuki, I.A. Fallis, S.J.A. Pope, J. Organometall. Chem. 749 (2014) 150.
[28] Y. Pellegrin, M. Sandroni, E. Blart, A. Planchat, M. Evain, N.C. Bera, M. Kayanuma, M. Sliwa, M. Rebarz, O. Poizat, C. Daniel, F. Odobel, Inorg. Chem. 50 (2011) 11309.
[29] M. Stephenson, C. Reichardt, M. Pinto, M. Wachtler, T. Sainuddin, G. Shi, H. Yin, S. Monro, E. Sampson, B. Dietzek, S.A. McFarland, J. Phys. Chem. 118 (2014) 10507.
[30] D. Tordera, A. Pertegas, N.M. Shavaleev, R. Scopelliti, E. Orti, H.J. Bolink, E. Baranoff, M. Gratzel, M.K. Nazeeruddin, J. Mater. Chem. 22 (2012) 19264.
[31] N. Armaroli, L. De Cola, V. Balzani, J.P. Sauvage, C.O. Dietrich-Buchecker, J.M. Kern, J. Chem. Soc. Faraday. Trans. 88 (1992) 553.
[32] M.S. Henry, M.Z. Hoffman, J. Phys. Chem. 83 (1979) 618.
[33] M.J. Frisch, G.W. Trucks, H.B. Schlegel, G.E. Scuseria, M.A. Robb, J.R. Cheeseman, G. Scalmani, V. Barone, B. Mennucci, G.A. Petersson, H. Nakatsuji, M. Caricato, X. Li, H.P. Hratchian, A.F. Izmaylov, J. Bloino, G. Zheng, J.L. Sonnenberg, M. Hada, M. Ehara, K. Toyota, R. Fukuda, J. Hasegawa, M. Ishida, T. Nakajima, Y. Honda, O. Kitao, H. Nakai, T. Vreven, J.A. Montgomery Jr., J.E. Peralta, F. Ogliaro, M. Bearpark, J.J. Heyd, E. Brothers, K.N. Kudin, V.N. Staroverov, R. Kobayashi, J. Normand, K. Raghavachari, A. Rendell, J.C. Burant, S.S. Iyengar, J. Tomasi, M. Cossi, N. Rega, N.J. Millam, M. Klene, J.E. Knox, J.B. Cross, V. Bakken, C. Adamo, J. Jaramillo, R. Gomperts, R.E. Stratmann, O. Yazyev, A.J. Austin, R. Cammi, C. Pomelli, J.W. Ochterski, R.L. Martin, K. Morokuma, V.G. Zakrzewski, G.A. Voth, P. Salvador, J.J. Dannenberg, S. Dapprich, A.D. Daniels, Ö. Farkas, J.B. Foresman, J.V. Ortiz, J. Cioslowski, D.J. Fox, Gaussian 09, Revision a. 1.Gaussian, Gaussian Inc, Wallingford, CT, 2009.
[34] E. Runge, E.K. Gross, Phys. Rev. Lett. 52 (1984) 997.
[35] S.L. Mayo, B.D. Olafson, W.A. Goddard, J. Phys. Chem. 94 (1990) 8897.
[36] P.C. Hariharan, J.A. Pople, Mol. Phys. 27 (1974) 209.
[37] M.S. Gordon, Chem. Phys. Lett. 76 (1980) 163.
[38] J.P. Perdew, K. Burke, M. Ernzerhof, Phys. Rev. Lett. 78 (1997) 1396.
[39] M.E. Casida, C. Jamorski, K.C. Casida, D.R. Salahub, J. Chem. Phys. 108 (1998) 4439.
[40] R.E. Stratmann, G.E. Scuseria, M.J. Frisch, J. Chem. Phys. 109 (1998) 8218.
[41] T. Lu, F.W. Chen, J. Comput. Chem. 33 (2012) 580.
[42] C. Hiort, P. Lincoln, B. Norden, J. Am. Chem. Soc. 115 (1993) 3448.
[43] Q.M. Wang, H. Tamiaki, J. Photochem. Photobiol. A 206 (2009) 124.
[44] P. Natarajan, M. Schmittel, Inorg. Chem. 52 (2013) 8579.
[45] G.C. Balazs, A. Guerzo, R.H. Schmehl, Photochem. Photobiol. Sci. 4 (2005) 89.